1

The Storfjorden, Svalbard Earthquake Sequence 2008-2020: Transtensional Tectonics in

an Arctic Intraplate Region

L. Ottemöller[1], W.-Y. Kim[2,3], F. Waldhauser[2], N. Tjåland[1] and W. Dallmann[4]

[1] Department of Earth Science, University of Bergen, Allegt.41, 5007 Bergen, Norway.

[2] School of Earth and Environmental Sciences, Seoul National University, Seoul, Korea.

[3] Lamont-Doherty Earth Observatory of Columbia University, Palisades, NY 10964, USA.

[4] Department of Earth Science, The Arctic University of Norway, Tromsø, Norway.

Corresponding author: Lars Ottemöller, Department of Earth Science, University of Bergen,

Allegt.41, 5007 Bergen, Norway, email: lars.ottemoller@uib.no

Conflict of interest statement: The authors acknowledge there are no conflicts of interest

recorded.

Abstract

An earthquake sequence in the Storfjorden offshore area southwest of Spitsbergen in the

Svalbard archipelago initiated with a magnitude M_W=6.1 event on 21 February 2008. This area

had previously not produced any significant earthquake, but between 2008 and 2020 a total of

~2,800 earthquakes were detected with ~16 of them being of moderate size ($M_L \geq 4.0$).

Applying double-difference relocation to improve relative locations reveals that the activity is

24   linked to several subparallel faults striking SW-NE that extend across the entire crust. The SW-

25   NE trend is also found as a possible fault plane from regional moment tensor inversion. The

26   solutions range from oblique-normal in the center of the cluster to pure strike slip further away,

27   and are consistent with the compressional σ_1 axis roughly in E–W direction and plunging 57º,

28   and extensional σ_3 axis sub-horizontal trending N–S. The mainshock fault is steeply dipping to

29   SE, but several other faults appear to be near vertical. The existence of oblique, right-lateral

30   strike-slip motion on SW-NE trending faults with normal component and pure normal faulting

31   events in-between suggests transtensional tectonics that in and around Storfjorden result in

32   activation of a complex fault system.

33

34   **Introduction**

35   A relatively strong earthquake of moment magnitude $M_W=6.1$ (Pirli et al., 2010)

36   occurred on 21 February 2008 offshore in Storfjorden between Spitsbergen and Edgeøya

37   (Figure 1 and 2). These islands and the Storfjorden constitute the Svalbard archipelago in the

38   Arctic region north of mainland Norway (Figure 1). The Svalbard region is situated in the

39   northwesternmost part of the Eurasian plate. Hence, the Svalbard archipelago is considered an

40   intraplate region (e.g., Mitchell et al, 1979). The earthquake was followed by an energetic

41   seismic sequence of ~2,800 detected events that is ongoing as of December 2020. About 2,050

42   events with local magnitude $M_L>1$ in the southern Storfjorden formed the central part of the

43   sequence within a rectangular area about 60 km wide and 70 km long (Figure 2). On 29 March

44   2016, a moderate-sized earthquake of $M_W=5.2$ (Global Centroid Moment Tensor (GCMT),

45   Ekström et al., 2012) occurred in the northeastern Storfjorden. This event was followed by

46   about 210 events ($M_L > 1$) mostly in 2016. Small shocks have also occurred onshore

47   northwestern Storfjorden, which is known as the Heerland region.

48   We refer to the activity as the '2008 Storfjorden earthquake sequence', as it contains a

49   number of moderate size events (~16 earthquakes with magnitude $M_L \geq 4$) that exhibit a more

50   complex spatio-temporal pattern than a typical main-aftershock sequence. The earthquake

51   sequence has been much more extensive and complex than would have been expected prior to

52   its onset based on the existing knowledge of faults in the Svalbard archipelago. Hardly any

53   earthquakes were detected offshore near the Storfjorden mainshock before 2008, going back to

54   when instrumental recording began. This earthquake sequence is also significant in that it is the

55   largest observed sequence of intraplate origin in Norway. The largest known intraplate events

56   on mainland Norway were the 1819 Lurøy (M = 5.8) and the 1904 Oslo fjord ($M_S = 5.4$)

57   earthquakes (Bungum et al., 2010). None of these events initiated prolonged aftershock activity.

58   Offshore Norway, large earthquakes occur regularly along the Jan Mayen fracture zone

59   (Rodriguez-Perez and Ottemöller, 2014) and along the Mid-Atlantic Ridge. Along the

60   Norwegian coast, seismic activity is moderate both in southern and northern Norway (Bungum

61   et al., 2010).

62   Previous work on the Storfjorden sequence described the first order structure and

63   kinematics of this ongoing intraplate seismicity and its temporal evolution (Pirli et al. 2010;

64   Pirli et al. 2013; Junek et al., 2014; Junek et al., 2015). They attributed the seismic activity to a

65   SW-NE trending fault system and a reactivated secondary structure beyond the mainshock fault

66   area. It was argued that the observed extensional stress is related to local sources. Junek et al.

67   (2014) computed moment tensor solutions based on a velocity model obtained through joint

68   receiver function and surface wave inversion and reported that the horizontal stresses do not

69   match the expected NW-SE compression from present day plate motion in the region (e.g.,

70   DeMets et al., 2010). Junek et al. (2015) used an event detection and grouping system to resolve

71   more detailed structures and concluded that the activity is attributed to NE-SW trending oblique

72   normal faults as well as NW-SE trending normal faults. However, the detailed geometry of the

73   secondary fault systems and their physical connection could not yet be resolved. It also remains

74   unclear how the Storfjorden activity and the causative tectonic processes fit into the regional

75   picture.

76   In this study, we compute high-precision earthquake locations and focal mechanisms to

77   image the fault system, with the goal to improve our understanding of the tectonics that control

78   the structure, evolution, and kinematics of this to-date on-going intraplate earthquake sequence.

79   We provide an update on the evolution of the earthquake sequence beyond 2012, the end of data

80   published by Junek et al. (2015), including the increase in activity in 2016 and that continues

81   today.

82

83   **Background**

84   *Seismicity*

85   The Svalbard region has experienced moderate levels of sparse seismicity since the

86   1970s as is typical for an intraplate region. However, several places in Svalbard exhibit

87   earthquake clusters with moderate-sized mainshocks. These areas are: Nordaustlandet (Chan

88   and Mitchell, 1985), Heerland, Spitsbergen (Mitchell et al. 1979) and Hopen Island (Ottemöller

89   et al. 2013) (Figure 2). There were two earthquakes with M>5 in the Svalbard region prior to

90   the start of the earthquake sequence in 2008. The first of them occurred on 18 January 1976

91   (mb=5.6) in the Heerland region on Spitsbergen (Figure 1). This event received some attention

92   due to its size and intraplate origin and, consequently initiated a temporary local monitoring

93   program (Bungum, 1977; Mitchell and Chan, 1978; Mitchell et al., 1979). The earthquake had a

94   strike-slip mechanism and Mitchell et al. (1990) suggested that the WNW-ESE striking nodal

95   plane was likely the fault plane, although it is different from known N-S trending major faults.

96   More recently, on 4 July 2003 an earthquake of M_W=5.4 occurred north of Hopen Island

97   (Figure 1; Ottemöller et al. 2013). Also the coastal area south of Hornsund has seen increased

98   activity since 2017 (Figure 2). In northern Svalbard, Nordaustlandet is the most active region

99   (Figure 2; Chan and Mitchell, 1985). More detailed descriptions of the seismic activity in the

100   1970s and 1980s are given in Bungum et al. (1982) and Mitchell et al. (1990).

101   *Tectonic Setting*

102   The source region of the Storfjorden earthquake sequence is mainly situated in southern

103   Storfjorden, which is the body of water between Spitsbergen and Edgeøya in the Svalbard

104   archipelago (Figure 1 and 2). The epicentral area is located in the northwestern part of the

105   Eurasian plate and it is considered as an intraplate region (e.g., Mitchel et al., 1979) even

106   though it is only about 250 km east of the seismically active Mid-Atlantic Ridge (Figure 1). On

107   its western side, the Svalbard continental crust transforms into oceanic crust across a narrow

108   continental margin. The Mid-Atlantic ridge in the region is the plate boundary between the

109   North American (NA) and Eurasian (EU) plates (Figure 1; Eldholm et al., 1990; Engen et al.

110   2003).

111   Most earthquakes on the spreading ridges are normal faulting and exhibit E-W trending

112   subhorizontal *T*-axes (Figure 1). Around the continental Svalbard archipelago, the ridge-push

113   force could result in approximatelty EW trending horizontal *P*-axis and near vertical *T*-axis.

114   But the *P*-axis for the 2008 Storfjorden mainshock trends E-W and plunges about 35º from the

115   vertical and the *T*-axis is near horizontal N-S trending (Figure 1; Pirli et al., 2010). In this broad

116   regional stress field, we expect oblique-normal or transtensional tectonics in the epicentral area.

117   Present day structural features of the Svalbard region stem from the break-up of the

118   Greenland plate from Svalbard and Eurasia due to seafloor spreading in the North Atlantic and

119   in the Arctic Ocean in Eocene (~52 Ma) (Eide, 2008). Continued seafloor spreading caused

120   development of a continental transform fault between Svalbard and Greenland and eventually,

121   the continental bridge between the two is broken at the end of Eocene (~33 Ma) and the

122   spreading continues until present day (Piepjohn et al., 2013). This Mid-Atlantic spreading ridge

123   exerts transtensional stress in the source region as discussed above.

124   The last significant geological event was the Pleistocene glaciation. Several times during

125   the last 2.5 million years, Svalbard was buried under glacial ice sheets.During the last glacial

126   maximum (~26 Ka), a continuous ice sheet covered most of Svalbard, the Barents Sea,

127   Scandinavia and large parts of north-eastern Europe (Landvik et al., 1998). The Strofjorden area

128   probably deglaciated around 15 Ka (e.g., Hormes et al., 2013). Total isostatic rebound in the

129   area has resulted in land uplift of ~145 m relative to sea level in Storfjorden (Winsborrow et al.,

130   1998; Hormes et al., 2013). Post-glacial isostatic uplift is still significant in eastern Svalbard

131   and the interior part of the Barents Sea (Forman et al., 2004).

132   Around the epicentral region, offshore southeastern Spitsbergen close to the Sørkapp,

133   there are NE-SW trending fault strands suggested in the seismic lines between Sørkapp and

134   Hopen (Bergh and Grogan, 2003). If such NE-SW trending faults exist around the epicentral

135   area, we expect oblique-normal faulting in the region due to N-S trending T-axis (see Figure 1).

136   It is also thought that two major N-S oriented fault zones, the Lomfjorden Fault Zone (LFZ) on

137   the western side of Storfjorden and the Storfjorden Fault Zone (SFZ) on the eastern side, extend

138   into the epicentral region. In addition, if the flexural stress due to removal of ice sheet plays a

139   role in the region, we may expect earthquake mechanisms that reveal such phenomena as

140 continental extension and oceanic compression due to different densities of continental and

141 oceanic lithospheres, and bending stress (Stein et al., 1989).

142

143 **Earthquake Location**

144   Seismicity in Svalbard is monitored closely by the Norwegian National Seismic

145 Network (NNSN) where stations belong to the NS and NO networks that are operated by

146 University of Bergen (UiB) and NORSAR, respectively (University of Bergen, 1982;

147 NORSAR, 1971; Ottemöller et al., 2021). There are seven seismographic stations in the region

148 (Table S1). An overview of the seismic stations in the region around Svalbard together with the

149 NNSN catalog locations is given in Figure 2, showing that 6 of them are within 300 km from

150 the mainshock area. The closest station HSPB is 80 km away from the cluster centroid.

151 However, a monitoring gap toward the northeast exists and the station HSPB was used for

152 routine detection by the NNSN only from November 2009. Following the mainshock on 21

153 February 2008, a total of ~2,800 earthquakes were detected and located by the NNSN in the

154 Storfjorden region until December 2020 (the distribution of NNSN location uncertainties is

155 given in Figure S2). The M_L scale used by the NNSN was developed by Alsaker et al. (1991)

156 for mainland Norway. This scale is also applied to the Storfjorden area because the wave

157 propagation paths are mostly in continental crust. We note that the M_L scale for Storfjorden

158 does not show signs of saturation as for the two largest events in the sequence on 21 February

159 2008 M_L(NNSN)=M_W(GCMT)=6.1 and on 29 March 2016 M_L(NNSN)=M_W(GCMT)=5.2. The

160 average number of events since 2008 was 210 each year, but 2010 and 2016 had nearly double

161 the number. The data set contains earthquakes from magntiude M_L=0.5 to 6.1.

162   The distribution of magnitude and the cumulative seismic moment are plotted in Figure

163 3. The main moment release (~90%) is attributed to the M_L=6.1 mainshock in 2008. The 2016

164 M_W=5.2 and 2010 M_W=4.9 earthquakes are clearly seen as a step in the cumulative moment.

165 The smaller events contribute to the gradual increase, and only earthquakes above M_L~ 4 are at

166 this scale noticed as a small step. The earthquake catalogue in this area is complete down to M_L

167 ~2.5 before mid 2009 and to ML ~2.2 thereafter. Using the M_L values from the complete data

168 set, we looked at the cumulative number of events as function of magnitude. From this we

169 obtain a b-value of 1.02 for the magnitude range M_L 2.5−6.1, where the cumulative event

170 number (N_c) is given by $\log 10 N_c = -1.02 \times M_L + 5.52$, following the Gutenberg-Richter law.

171   We used the HYPOCENTER location program (Lienert, 1994; Lienert and Havskov,

172 1995) together with first and secondary P and S phase arrival times routinely picked by the

173 NNSN to locate the earthquakes using the SEISAN software (Havskov et al., 2020). These

174 initial NNSN bulletin locations were obtained based on travel time calculations using the

175 default NNSN velocity model (Havskov and Bungum, 1987; Figure S1). The computed location

176 uncertainties for this data set are plotted as histograms in Figure S2. HYPOCENTER makes use

177 of the secondary phases (Pg and Sg) even if the first arrival (Pn or Sn) is not present, which is

178 the case for stations KBS and BJO1 for events in the Storfjorden region. We double-checked the

179 robustness of a subset of the HYPOCENTER locations by applying the HYPOINVERSE

180 program (Klein, 2007) to first-arrival data only and found no significant differences.

181   We constructed a 1D velocity model (STOR) for location purposes (Figure S1) from

182 various sources (Breivik et al., 2005; Czuba et al., 2008; Ritzmann et al., 2007). The model

183 overall features slightly higher velocities and produces lower RMS residuals compared to the

184 routine model used by the NNSN and models used in previous studies (Pirli et al., 2010). Our

185   model predicts observed Pg and Pn phases reasonably well, also beyond the cross-over distance

186   where Pg is observed as a secondary phase. We used this model to relocate the earthquakes

187   from the NNSN bulletin using HYPOCENTER before applying the double-difference

188   reloaction. The mean RMS travel time residual of all events is 5% lower for our model

189   compared to the default model used by the NNSN.

190

191   **Hypocenter relocation**

192   We utilized the double-difference method (Waldhauser and Ellsworth, 2000), as

193   implemented in the hypoDD program (Waldhauser, 2001), to improve the relative locations of

194   events within the sequence. We used a total of ~1.4 million P and ~1.2 million S travel-time

195   differences formed from first arrival phase picks to relocate a total of ~2,800 earthquakes in an

196   iterative weighted least-squares procedure that solves for adjustments in event separations

197   (Waldhauser and Ellsworth, 2000). A continuous chain of linked events with at least 6 delay

198   time observations was required, resulting in the robust relocation of 84% of the total number of

199   events. The velocity model used for relocation is plotted in Figure S1.

200   Epicenters of the 2,321 relocated earthquakes (Figure 4) are mostly distributed within a

201   100 x 170 km elongated, SW-NE trending seismic zone. Hypocenter depths cover much of the

202   crust down to 30 km. Compared to the routine NNSN and the initial HYPOCENTER locations

203   (Figure 2), the relocated seismicity more clearly delineates several structural features that were

204   activated during the course of the earthquake sequence. Histograms of change in epicenter

205   location and depth from NNSN bulletin to hypoDD relocation are given in Figure S3. In

206   addition to the overview (Figure 4), the double difference results are used to present the

207   different stages of the sequence in time (Figure 5) and to show profiles across selected fault

208 lines identified from the seismicity (Figure 6). In these figures, the same color code is applied to

209 indicate the year of the earthquakes. The seismicity in Figures 4 and 5 is plotted together with

210 the fault plane solutions that will be explained later.

211

212 **Regional moment tensor solutions and local stress orientation**

213 We determined source mechanisms of the large earthquakes in the sequence ($M_W \geq 3.9$)

214 by using the regional waveform modeling and moment tensor inversion method developed by

215 Dreger (2003). We constrained the focal depth by inverting for moment tensor for a range of

216 depths and selecting the depth that yields the highest variance reduction and double-couple

217 percentage. The waveforms were modelled based on the Barents3D model (Ritzmann et al.,

218 2007; Figure S1) for the Storfjorden area and stations within about 400 km were used (Figure

219 1). An example of the moment tensor inversion waveforms and results is given in Figure S4.

220 We note that the moment tensor inversion was rather stable with respect to various hypocenter

221 depths in the inversion and obtained 14 robust regional moment tensor solutions (Table 1,

222 Figure 7a). In addition to the fault plane solutions determined here, we used the GCMT solution

223 for the mainshock, as well as 12 April 2010 and 29 March 2016 events, and two solutions

224 provided by Pirli et al. (2013) (Table 1). The moment tensor solutions of several events

225 determined here are common to previous solutions by GCMT, Pirli et al (2010, 2013), and

226 Junek et al. (2013) and being consistent gives us confidence in our solutions. The last moment

227 tensor solution from the sequence is from 2017 as no large enough events occurred since then.

228 Our depth estimates place the earthquakes into the basement rocks within the depth range of

229 about 10 to 20 km. However, the uncertainties in the velocity model combined with sparse

230 station coverage result in an uncertainty of about 5 km in the depth estimates.

231   To assess the state of stress in the Storfjorden area, the focal mechanisms of the 19

232   events given in Table 1 were inverted for the local stress tensor (Gephart & Forsyth, 1984;

233   Michael, 1987). Based on plunges of *P* and *T* axes, ten events are strike-slip, six events are

234   normal faulting, and three events are oblique-normal (Table 1; Figure 7a). 88% of the *T* axes

235   trend within ±17º from NNW-SSE (~350º), and the *P* axes trend nearly E-W (~260º ± 20º).The

236   method performs a grid search to find the best-fit stress tensor, which can be described by three

237   principal stress directions and a measure of the relative sizes of the principal stresses, referred to

238   as the stress ratio, R, defined as, $R = (\sigma_2 - \sigma_1)/(\sigma_3 - \sigma_1)$ (Gephart and Forsyth, 1984). The

239   principal constraint in the inversion is that the shear stress direction on any fault plane must

240   coincide with the observed slip direction in both orientation and sign (Gephart and Forsyth,

241   1984). We searched the whole model space with 5º intervals and within the variance of 15º, and

242   the datum with large uncertainty in the double-couple mechanisms were weighted down in the

243   inversion.

244   The results of the stress inversion are plotted in Figure 7b. The stereonet plot indicates

245   the trends and plunges of σ_1 and σ_3 axes of local stress models within 95% confidence limit.

246   The stress axes shown on the plot indicate those for which at least one stress model was found.

247   The best-fitting model using the minimum rotation criterion has an average misfit of only about

248   2.6º, or well within the uncertainty of the observations, indicating a good fit to the data set. The

249   σ_3 is subhorizontal (plunge = 14º) and trends NNW-SSE (trend = 159º). The result of the stress

250   inversion indicates that the greatest principal stress axis (σ_1) trends EW (272º) with a moderate

251   plunge of 57º indicating an oblique extensional stress regime in the Storfjorden region.

252

253 **Spatio-temporal evolution of seismicity**

254   We analyzed the detailed spatio-temporal pattern of the 2008 Storfjorden sequence to

255 learn about the seismotectonics of Storfjorden (Figure 5). The sequence started with the

256 M_W=6.1 mainshock on 21 Feb 2008, featuring oblique, right-lateral strike slip motion with

257 significant normal faulting component on a steeply dipping fault (Figures 4,5 and 6). This

258 mainshock was followed by many events in the first 50 days, including three moderate size

259 earthquakes for which moment tensor solutions were computed (Table 1; Figure 4 and 5). This

260 initial activity occurred around the mainshock. Subsequent earthquakes that include a strike-slip

261 faulting event are distributed on the central and NE quadrant of the seismic zone (Figure 5a).

262 The SW-NE strike direction of the mainshock matches the alignment of earthquakes along

263 feature A in Figure 5a. The SE dipping fault plane from the mainshock can be seen in the

264 projection plane that is perpendicluar to A (Figure 6a). However, seismicity around the

265 mainshock is complex and the fault is not sharply defined. Most of the earthquakes follow the

266 mainshock within the first several months, with fewer events occurring in 2009 and up to 11

267 April 2010 (Figure 5a).

268   The large earthquake of M_W=4.9 occurred on 12 April 2010 in the central part of the

269 seismic zone on the same fault activated by the mainshock (A in Figure 5a and 5b). It has a

270 similar mechanism as the mainshock – oblique-normal faulting (Table 1, Figure 5b). Numerous

271 small earthquakes followed this event, predominately activating a clearly defined near vertical

272 structure (B in Figure 5b) that is in the SW quadrant with a slight offset from the mainshock

273 fault A. The fault trace B is subparallel to the mainshock fault A and appears as a SW step-over

274 from it. The projection plane for B (Figure 6b) suggests that this near vertical fault cuts through

275 the entire crust. The projection plane further north (Figure 6c) shows the main fault A, but also

276   the parallel feature E to the west (Figure 5b). Acivity is also on another short fault (D in Figure

277   5b) that runs subparallel to the main fault. Among the larger events in 2010-2011 are three pure

278   normal faulting earthquakes. The activity continued throughout 2010 and 2011, but by the end

279   of 2011 the seismic activity had subsided from previous levels.

280   Between 2012 and 2015 events predominately clustered near the 2008 mainshock. In

281   2013, earthquakes started to appear on a previously inactive feature F (Figure 5c) NW of the

282   main cluster. There is a clear gap between the main cluster A and this feature F. The earthquake

283   on 21 November 2013 near F has a right-lateral NNE striking pure strike-slip mechanism.

284   During this time interval, a number of events started to appear onshore Spitsbergen further north

285   (G in Figure 4). This area is close to the moderate sized Heerland earthquake in 1976 (Figure 1;

286   Mitchell et al., 1990).

287   The most significant development during the time period 2016-2020 was the occurrence

288   of earthquakes offshore western Edgeøya (Figures 2 and 4). This area became active with two

289   earthquakes of magnitude M_W=5.2 and M_L=4.9, respectively, only 28 seconds apart on 29

290   March 2016. Hundreds of smaller earthquakes occurred around the 2016 shock, and it appears

291   that it is a distinct cluster that is largely seperated from the 2008 mainshock area. The cluster

292   appears to be diffuse (H in Figure 4), however, the cross-section perpendicular to H reveals

293   near vertical fault planes (Figure 6d). The mechanism of the M_W=5.2 2016 earthquake is right-

294   lateral strike-slip faulting on a NE striking vertical fault matching the orientation of the

295   seismicity (Figure 4 and 6d). Several of the previously active structures (A, B, E, F in Figure

296   5d) remained active during this period. Moment tensor solutions were obtained for two events

297   with M_W>4 in 2017 near the 2008 mainshock. The solutions were normal and oblique normal,

298   respectively.

299

Discussion

301   The Storfjorden earthquake sequence that started in 2008 and still continues in 2020

302   came as a surprise in terms of earthquake size, spatial extent and possible tectonic causes as no

303   significant seismicity had been noticed in the area prior to its onset. Results from previous

304   studies (Pirli et al., 2013; Junek et al., 2015) were consistent in locating the seismicity and

305   providing moment tensor solutions for the activity until 2012. The general fault trend was

306   identified as NE-SW with oblique-normal mechanisms with connecting normal faults in NW-

307   SE direction. Both Pirli et al. (2013) and Junek et al. (2015) favour local stress sources as the

308   underlying cause

309   In this study we extend the observational period and study the evolution of the

310   earthquake seqeuence until 2020 (Figures 4, 5 and 6). The central part of the sequence (A in

311   Figure 4 and 5) remained active throughout the sequence and most of the larger events ($M_L{\geq}4$)

312   have occurred there. Within about 50 km from the mainshock and the surrounding cluster A, the

313   clusters B-F (Figure 5) are independent and largely separated in space. About 100 km further

314   north clusters G and H started to developed in 2013 and 2016, respectively. The second largest

315   event of the sequence (M_W=5.2 on 29 March 2016) falls into cluster H. With the large spatial

316   separation it may be questionable if the entire Storfjorden activity should be seen as one

317   sequence. However, the continual increase in spatial extent from the mainshock since 2008 may

318   suggest this to be the case, and it is possible that the sequence is caused by regional scale

319   tectonic processes and related stresses. However, local stress sources may also play a role as

320   suggested by Pirli et al. (2013) and Junek et al. (2015).

321   We aimed at resolving the complexity of the fault system by applying the double

322   difference relative location approach to the seismic data. This resulted in better locations of

323   events in specific clusters (e.g. F, Figure 5) and a general sharpening of the seismicity compared

324   to the routine catalog (Figure 2). The majority of the events (about 80%) are located between 5

325   and 25 km depth (Figure 6), which means the activity is spread over much of the brittle crust.

326   The activity is rather complex in the main cluster, but we are able to identify specific faults

327   from the seismicity maps (Figure 4 and 5) that can also be traced in the projection planes

328   (Figure 6).

329   We performed moment tensor inversion for many of the larger events in the sequence

330   and obtained robust results (Figure 4 and 7). The results are stable with respect to changes in the

331   velocity model or hypocenter depth, and also consistent with previous results (Pirli et al., 2013;

332   Junek et al., 2015). We find that mechanisms are predominantly oblique-normal around the

333   main cluster A. We favour the SW-NE strike as the causative fault plane as the seismicity

334   appears to be generally elongated in this direction (Figure 5 and 6). However, some more purely

335   normal faults are also present in the central part as well as in cluster B. Moving farther away,

336   most of the mechanisms are pure strike-slip on near vertical fault plane and right-lateral

337   displacement along the SW-NE striking fault.

338   The diversity of focal mechanisms, especially within the SW structures, are indicative of

339   a complex fault geometry. It is likely that the individual near-vertical NW-SE faults are offset

340   from each other, and possibly connected by perpendicular normal faults. The principal direction

341   of stress expected in the Storfjorden seismic zone is a compressive horizontal force from the

342   mid-Atlantic spreading ridge due to present day plate motion with a NW-SE direction.

343   However, the local greatest principal stress (σ_1) determined in this study trends EW at a plunge

344   of 57º (Figure 7) and the least principal stress (σ_3) trends almost NS. In this case, the crustal

345   deformation in this region is accommodated along subparallel strike-slip and dip-slip faults.

346   Hence, the deformation is transtensional (oblique-extensional) tectonics (e.g., Wesnousky and

347   Jones, 1994).

348

349   **Conclusions**

350   We conclude that the Storfjorden earthquake sequence is attributed to a complex fault

351   system that has evolved and grown since its onset in 2008. It started with a large M_L=6.1

352   earthquake that until 2020 was followed by ~2,800 detected events, with ~16 of them of $M_L \geq 4$.

353   Relative relocation has provided a sharpened image of the seismicity allowing identification of

354   fault segments that are mostly striking SW-NE. Event depths appear to be spread over much of

355   the crust. Moment tensor inversion has revealed predominantly oblique-normal faulting

356   mechanisms on SW-NE trending steeply dipping faults, but half dozen normal faulting events

357   show their nodal planes perpendicular to the NE-SW trending major structures. Further away

358   from the mainshock cluster, several earthquakes show predominantly strike-slip mechanisms on

359   near vertical fault plane with NE-SW strikes. The inferred stress field in the Storfjorden region

360   revealed from the earthquake sequence gives the σ_1 axis roughly in EW direction at a plunge of

361   57º. The least principal stress (σ_3) is sub-horizontal and trends N-S and acts as the extensional

362   stress axis. The main orientation of faults in SW-NE direction with oblique-normal slip is

363   consistent with transtensional deformation. The deformation in the Storfjorden area could be the

364   result of regional tectonic forces, although local sources cannot be ruled out.

365

366   **Data and resources**

367   We used data from seismic stations as indicated in Table S1. The stations belong to the

368   following networks: NS (https://doi.org/10.7914/SN/NS), NO (doi: 10.21348/d.no.0001), PL

369   (https://www.fdsn.org/networks/detail/PL/) and IU (https://doi.org/10.7914/SN/IU). Waveform

370   data from the NS and NO network can be extracted from the UIB-NORSAR EIDA node

371   (Ottemöller et al., 2020; https://eida.geo.uib.no/).

372   The events with the phases are included in the Norwegian National Seismic Network

373   earthquake catalog, which can be downloaded at http://nnsn.geo.uib.no/nnsn/#/data/events

374   All figures in this paper are prepared with the Generic Mapping Tools (Wessel et al., 2019).

375   The hypoDD software can be obtained at https://www.ldeo.columbia.edu/~felixw/hypoDD.html

376   (last accessed 16 March 2021).

377

388

389
390   **References**

391

392   Albuquerque Seismological Laboratory (ASL)/USGS. (1988). Global Seismograph Network

393   (GSN - IRIS/USGS). International Federation of Digital Seismograph Networks.

394   https://doi.org/10.7914/SN/IU

395   Alsaker, A., R. Kvamme, R. A. Hansen, A. Dahle, and H. Bungum (1991). The ML scale in

396   Norway, *Bull. Seismol. Soc. Am.*, 81, 379–398.

397   Atkinson, G. M., and D.M. Boore (2006). Earthquake Ground-Motion Prediction Equations for

398   Eastern North America, *Bull. Seismol. Soc. Am.*, 96, 2181–2205.

399   Bergh, S. G., and P. Grogan (2003). Tertiary structures of the of the Sørkapp-Hornsnd Region,

400   South Spitsbergen, and implications for the offshore southern extension of the fold-

401   thrust belt, *Norsk Geologisk Tidsskrift*, 83, 43–60.

402   Breivik, A. J., R. Mjelde, P. Grogan, H. Shimamura, Y. Murai, Y., and Y. Nishimura (2005).

403   Caledonide development offshoreonshore Svalbard based on ocean bottom seismometer,

404   conventional seismic, and potential field data, *Tectonophysics*, 401, 79–117.

405   Brothers, D. S., N. W. Driscoll, G. M. Kent, A. J. Harding, J. M. Babcock, and R. L. Baskin

406   (2009). "Tectonic evolution of the Salton Sea inferred from seismic reflection data."

407   Nature Geoscience 2, no. 8, 581–584.

408   Bungum, H. (1977). Two focal-mechaism solutions for earthquakes from Iceland and Svalbard,

409   *Tectonophysics*, 41, T15–T18.

410   Bungum, H., B.J. Mitchell, and Y. Kristoffersen (1982). Concentrated earthquake zones in

411   Svalbard, *Tectonophysics*, 82, 175–188.

412   Bungum, H., O. Olesen, C. Pascal, S. Gibbons, C. Lindholm, and O. Vestø (2010). To what

413   extent is the present seismicity of Norway driven by post-glacial rebound?, *Journal of*

414   *the Geological Society, London*, 167, 373–384.

415   Chan, W. W., and B. Mitchell (1985). Intraplate earthquakes in northern Svalbard,

416   *Tectonophysics*, 114, 181–191.

417   Czuba, W., M. Grad, A. Guterch, M. Majdanski, M. Malinowski, R. Mjelde, M. Moskalik, P,

418   Sroda, M. Wilde-Piorko, and Y. Nishimura (2008). Seismic ctrustal structure along the

419   deep transect Horsted'05, Svalbard, Polish Polar Research, 29, 279–290.Dahle, A.,

420   Bungum, H., and Kvamme, L. B., 1990. Attenuation models inferred from intraplate

421   earthquake recordings, *Earthq. Eng. Struct. Dyn.*, 19, 1125–1141.

422   DeMets, C., R.G. Gordon, and D.F. Argus (2010). Geologically current plate motions, *Geophys.*

423   *J. Int.*, *181*, 1-80, doi: 10.1111/j.1365-246X.2009.04491.x, 2010; see also Erratum,

424   *Geophys. J. Int.*, *0*, 1-1, doi: 10.1111/j.1365-246X.2011.05186.x, 2011.

425   Dreger, D. S. (2003). TDMT INV: Time Domain Seismic Moment Tensor INVersion, in

426   *International Handbook of Earthquake and Engineering Seismology*, edited by W. H. K.

427   Lee, H. Kanamori, P. C. Jennings, and C. Kisslinger, vol. 81B, p. 1627, IASPEI,

428   Academic Press.

429   Dziewonski, A.M., T.-A. Chou, and J.H. Woodhouse (1981). Determination of earthquake

430   source parameters from waveform data for studies of global and regional seismicity, *J.*

431   *Geophys. Res.*, 86, 2825–2852.

432   Eide, E. E. (2002). BATLAS – Mid-Norway Plate Reconstruction Atlas with Global and

433   Atlantic Perspectives. Geological Survey of Norway.Ekström, G., M. Nettles, and A.M.

434   Dziewonski (2012). The global CMT project 2004-2010: Centroid-moment tensors for

435   13,017 earthquakes, *Phys. Eartg Plan. Int.*, 200, 1–9.

436   Eldholm, O., A. M. Karasik, and P. A. Reksnes (1990). The North American plate boundary, in

437   The Geology of North America, vol. L, The Arctic Ocean Region, editors A. Grantz et

438   al., pp. 171– 182, *Geol. Soc. of Am.*, Boulder, Colorado.Engen, Ø., O. Eldholm, and H.

439   Bungum (2003). The Arctic plate boundary, *J. Geophys. Res.* 108, 2075, doi:

440   https://doi.org/10.1029/2002JB001809.

441   Forman, S. L., D.J. Lubinski, O. Ingolfsson, J.J. Zeeberg, J.A. Snyder, M.J. Siegert, and G.G.

442   Matishov (2004). A review of postglacial emergence on Svalbard, Franz Josef Land and

443   Novaya Zemlya, northern Eurasia, *Quaternary Science Reviews*, 23, 1391–1434.

444   Gephart, J. W. (1990). FMSI: a FORTRAN program for inverting fault/slikenside and

445   earthquake focal mechanism data to obtain the regional stress tensor, *Computers &*

446   *Geosciences*, 16, 953–989.

447   Gephart, J. W., and D.W. Forsyth (1984). An improved method for determining the regional

448   stress tensor using earthquake focal mechanism data: Application to the San Fernando

449   earthquake sequence, *J. Geophys. Res.*, 89, 9305–9320.

450   Havskov, J., and H. Bungum (1987). Source parameters for earthquakes in the northern North

451   Sea, *Norsk Geologisk Tidsskrift*, 67, 51–58.

452   Havskov J., P.H. Voss, and L. Ottemöller (2020). Seismological Observatory Software: 30 yr of

453   SEISAN, *Seismol. Res. Lett.*, doi: https://doi.org/10.1785/0220190313.

454   Hormes, A., E.F. Gjermundsen, and T.L. Rasmussen (2013). From mountain top to the deep sea

455   — deglaciation in 4D of the northwestern Barents Sea, *Quarternary Science Reviews*,

456   75, 78–99.

457   Junek, W. N., J.I. Roman-Nieves, and M.T. Woods (2014). Tectonic implications of earthquake

458   mechanisms in Svalbard, *Geophys. J. Int.*, 196, 1152–1161.

459   Junek, W.N., T. Kværna, M. Pirli, J. Schweitzer, D.B. Harris, D.A. Dodge, and Woods M.T.

460   (2015). Inferring aftershock sequence properties and tectonic structure using empirical

461   signal detectors. *Pure and Applied Geophysics* 172, 359373.

462   Klein, F. W. (2007). Users Guide to HYPOINVERSE2000, a Fortran program to solve for

463   earthquake locations and magnitudes, *U.S. Geological Survey Open-file Report*, 02-171,

464   121 pp.

465   Landvik, J. Y., S. Bondevik, A. Elverøi, W. Fjeldskaar, J. Mangerud, O. Salvigsen, M.J.

466   Siegert, J.I. Svendsen, and T.O. Vorren (1998). The last glacial maximum of Svalbard

467   and the Barents Sea area: Ice sheet extent and configuration, *Quarternary Science*

468   *Reviews*, 17, 43–75.

469   Lienert, B. R. (1994). Hypocenter 3.2: A computer program for locating earthquakes locally,

470   regionally and globally, Tech. rep., Hawaii Institute of Geophysics & Planetology,

471   Honolulu.

472   Lienert, B. R., and J. Havskov (1995). A computer program for locating earthquakes both

473   locally and globally, *Seis. Res. Lett.*, 66, 26–36.

474   Michael, A. J. (1987). Use of focal mechanisms to determine stress: A control study, *J.*

475   *Geophys. Res.*, 92, 357–368.

476   Mitchell, B. J.. and W.W.W. Chan (1978). Characteristics of earthquakes in the Heerland

477   seismic zone of Eastern Spitsbergen, *Polarforschung*, 48, 31–40.

478   Mitchell, B. J., J.E. Zollweg, J.J. Kohsmann, C.-C. Cheng, E.J. and Haug (1979). Intraplate

479   earthquakes in the Svalbard Archipelago, *J. Geophys. Res.*, 84, 5620–5626.

480   Mitchell, B. J., H. Bungum, W.W. Chan, P.B. and Mitchell (1990). Seismicity and present-day

481   tectonics of the Svalbard region, *Geophys. J. Int.*, 102, 139–149.

482   NORSAR (1971). NORSAR Station Network [Data set], https://doi.org/10.21348/d.no.0001.

483   Ottemöller, L., and J. Havskov (2003). Moment magnitude determination for local and regional

484   earthquakes based on source spectra, *Bull. Seismol. Soc. Am.*, 93, 203–214.

485   Ottemöller, L., B.M. Storheim, K. Atakan, J. Havskov, and M.B. Sørensen (2013). Norwegian

486   National Seismic Network: Decade report 2001-2010, Scientific report, Department of

487   Earth Science, University of Bergen, Bergen, Norway,

488   Ottemöller, L., J. Michalek, J.-M. Christensen, U. Baadshaug, F. Halpaap, Ø. Natvik, T.

489   Kværna, and V. Oye (2021). UiB-NORSAR EIDA Node: Integration of Seismological

490   Data in Norway, *Seis. Res. Lett.*, doi: https://doi.org/10.1785/0220200369

491   Piepjohn, K., W. von Gosen, A. Läufer, W.V. McClelland, and S. Estrada (2013), Ellesmerian

492   and Eurekan fault tectonics at the northern margin of Ellesmere Island (Canadian High

493   Arctic), *Z. Dt. Ges. Geowiss* **164**(1), 81-105.

494   Piepjohn K., W.K. Dallmann, and S. Elvevold (2019). The Lomfjorden Fault Zone in eastern

495   Spitsbergen (Svalbard). The Geological Society of America Special Paper 541, 95-130.

496   Pirli, M., J. Schweitzer, L. Ottemöller, M. Raeesi, R. Mjelde, K. Atakan, A. Guterch, S.J.

497   Gibbons, B. Paulsen, W. Debski, P. Wiejacz, and T. Kværna (2010). Preliminary

498   analysis of the 21 February 2008 Svalbard (Norway) seismic sequence, *Seis. Res. Lett.*,

499   81, 63–75.

500   Pirli, M., J. Schweitzer, and B. Paulsen (2013). The Storfjorden, Svalbard, 2008-2012

501   aftershock sequence: Seismotectonics in a Polar envrionment, *Tectonophysics,* 192-205.

502 Ritzmann, O., N. Maercklin, J.I. Faleide, H. Bungum, W.D. Mooney, and S.T. Detweiler

503   (2007). A three-dimensional geophysical model of the crust in the Barents Sea region:

504   model construction and basement characterization, *Geophys. J. Int.*, 170, 417–435.

505 Rodríguez-Pérez Q., and Ottemöller L. 2014. Source study of the Jan Mayen transform fault

506   strike-slip earthquakes, *Tectonophysics* 628, 71–84.

507 Shapiro, N. M., and M.H. Ritzwoller (2002). Monte-Carlo inversion for a global shear velocity

508   model of the crust and upper mantle, *Geophys. J. Int.*, 151, 88–105.

509 Stein, S., S. Cloetingh, N.H. Sleep, and R. Wortel (1989), Passive Margin Earthquakes, Stresses

510   and Rheology, *in* S. Gregersen and P. W. Basham, *eds*, *Earthquakes at North- Atlantic*

511   *Passive Margins: Neotectonics and Postglacial Rebound*, Kluwer Academic Publishers,

512   pp. 231-259.

513 University Of Bergen (1982). University of Bergen Seismic Network [Data set]. International

514   Federation of Digital Seismograph Networks. https://doi.org/10.7914/SN/NS

515 Waldhauser, F. (2001). hypoDD – A program to compute double-difference hypocenter

516   locations, Tech. Rep., U.S. Geol. Survey, Menlo Park, CA.

517 Waldhauser, F. and W.L. Ellsworth (2000). A double-difference earthquake location algorithm:

518   Method and application to the Northern Hayward Fault, California, *Bull. Seismol. Soc.*

519   *Am.*, 90, 1353–1368.

520 Wesnousky, S.G., and C. H. Jones (1994). Oblique slip, slip partitioning, spatial and temporal

521   changes in the regional stress field, and the relative strength of active faults in the Basin

522   and Range, western United States, *Geology*, **22**, 1031-1034.

523   Wessel, P., J.F. Luis, L. Uieda, R. Scharroo, F. Wobbe, W.H.F. Smith, and D. Tian (2019). The

524   Generic Mapping Tools version 6. Geochemistry, Geophysics, Geosystems, 20, 5556–

525   5564. https://doi.org/10.1029/2019GC008515

526   Winsborrow, M. C. M., K. Andreassen, G.D. Corner, and J.S. Laberg (1998). Deglaciation of a

527   marine-based ice sheet: Late Weichselian paleo-ice dynamics and retreat in the southern

528   Barents Sea reconstructed from onshore and offshore glacial geomorphology,

529   *Quarternary Science Reviews*, 29, 424–442.

530

531   **Author mailing addresses:**

532

533   Lars Ottemöller

534   Department of Earth Science

535   University of Bergen

536   Allegt.41

537   5007 Bergen

538   Norway

539

540   Won-Young Kim

541   School of Earth and Environmental Sciences, Seoul National University, Seoul, Korea

542   On Leave from:

543   Lamont-Doherty Earth Observatory of Columbia University

544

545   61 Route 9W

546   Palisades

547   NY 10964-1000

548   USA

549

550   Felix Waldhauser

551   Lamont-Doherty Earth Observatory of Columbia University

552

553   61 Route 9W

554   Palisades

555   NY 10964-1000

556   USA

557

558   Norunn Tjåland

559   Department of Earth Science

560   University of Bergen

561   Allegt.41

562   5007 Bergen

563   Norway

564

565   Winfried Dallmann

566   Department of Earth Science

567   The Arctic University of Norway

568   Postboks 6050 Langnes

569   9037 Tromsø

570   Norway

571

572
573

574

575

576   Table 1. Focal mechanism of earthquakes during the 2008 Storfjorden sequence[†]. Solutions that

577   were not obtained in this study are shaded in gray, see annoation for details. Note that the

578   second nodal planes can be seen in Figure 4.

579

Id	Date (yr-mo-dy)	Time (h:m:s)	Lat. (ºN)	Long. (ºE)	h (km)	Mag (Mw)	ϕ (°)	δ (°)	λ (°)	DC (%)	FM
1	2008-02-21[‡]	02:46:18	76.987	18.912	14	6.1	53	71	-141	84	SN
2	2008-02-21	22:52:41	76.969	18.931	18	4.0	20	68	-157	87	SS
3	2008-02-29	08:16:07	77.272	20.212	17	3.9	47	75	-146	61	SS
4	2008-04-10	06:20:03	77.022	19.140	16	4.2	40	64	-133	96	SN
5	2009-11-23	19:07:49	77.123	18.357	17	4.3	23	66	-159	99	SS
6	2010-01-13	10:08:21	76.972	18.298	11	4.3	131	51	-66	84	NF
7	2010-04-12[‡]	07:57:22	76.966	18.884	20	4.9	34	57	-140	73	SN
8	2010-09-15§	05:56:33	76.861	18.134	5	4.1	74	53	-105	99	NF
9	2010-09-22§	06:56:50	76.871	18.174	6	4.0	39	71	-161	99	SS
10	2010-11-16	22:00:51	76.888	18.321	11	4.3	104	35	-104	32	NF
11	2011-01-22	11:25:11	76.955	18.762	14	4.4	20	64	-164	98	SS
12	2011-05-05	11:09:05	77.046	18.988	15	4.3	31	54	-138	99	NF
13	2011-10-02	20:54:44	77.391	20.035	10	4.0	213	86	-174	83	SS
14	2013-07-27	16:22:53	76.916	18.107	15	4.2	55	53	-134	28	NF
15	2013-11-21	21:38:31	77.210	17.727	11	4.1	23	75	177	51	SS
16	2014-04-24	08:33:07	76.960	18.691	11	3.9	55	60	-156	92	SS
17	2016-03-29[‡]	10:32:10	77.79	20.43	11	5.2	224	89	-171	67	SS
18	2017-07-16	04:49:26	77.044	18.786	13	4.0	246	53	-103	78	NF

| 19 | 2017-12-31 | 15:50:24 | 76.983 | 18.835 | 13 | 4.3 | 18 | 74 | -157 | 77 | SS |

580

581 † h= focal depth; ϕ = strike, δ = dip, λ= rake; DC = double-couple percentage; FM = focal mechanism

582 type, SN = oblique-normal; SS=strike-slip mechanism; NF=normal faulting;

583 ‡ moment tensor from the Global Centroid Moment Tensor (Dziewonski et al., 1981; Ekström et
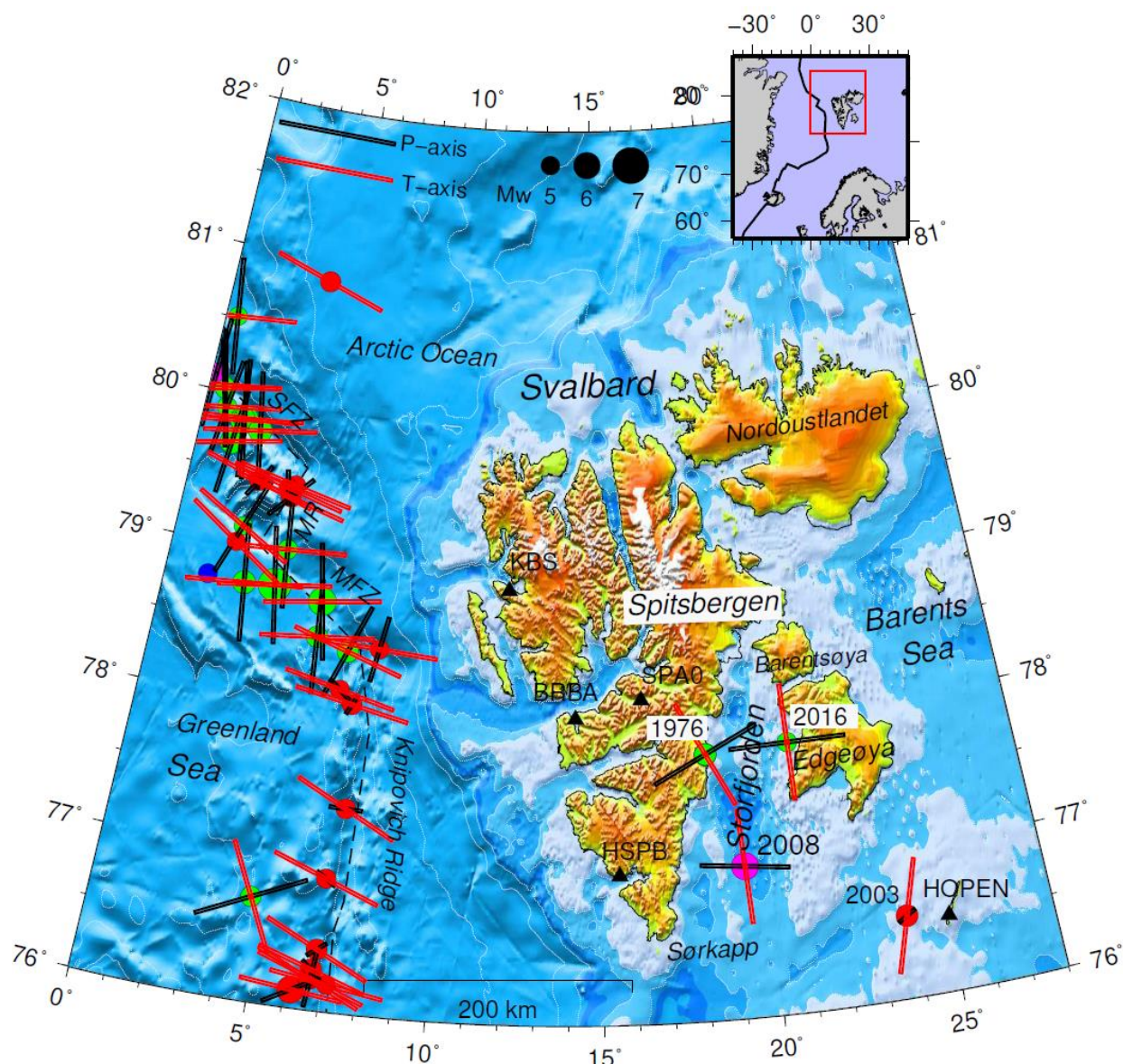
584 al., 2012)

585 § focal mechanism and depth from Pirli et al. (2013)

586 ¶ focal mechanism and depth from Mitchell et al. (1990)

587

588

589

591   Figure 1. Earthquakes that occurred during 1976 – 2020 obtained from the Global CMT catalog

592   are plotted with circles and seismographic stations are plotted by triangles. Circle size is

593   proportional to the seismic moment of each event, and color coded for focal mechanism types:

594   red= normal faulting, green= strike-slip, blue= thrust, and magenta= oblique-normal faulting.

595   Earthquakes with Mw > 5 are plotted, and the horizontal projection of P-axis (black bar), and *T*-

596   axis (red bar) of each earthquake are plotted. Near vertical *P*-axis is plotted with a short black

597   bar, whereas horizontal *P*- and T-axes are plotted with full scale black and red bars,

598   respectively, as shown upper left.Red rectangular box in the inset legend map indicates the

599   region around Svalbard archipleago. Significant events that are discussed in the text are labeled

600   with the respective years 1976, 2003, 2008 and 2016.

601

602
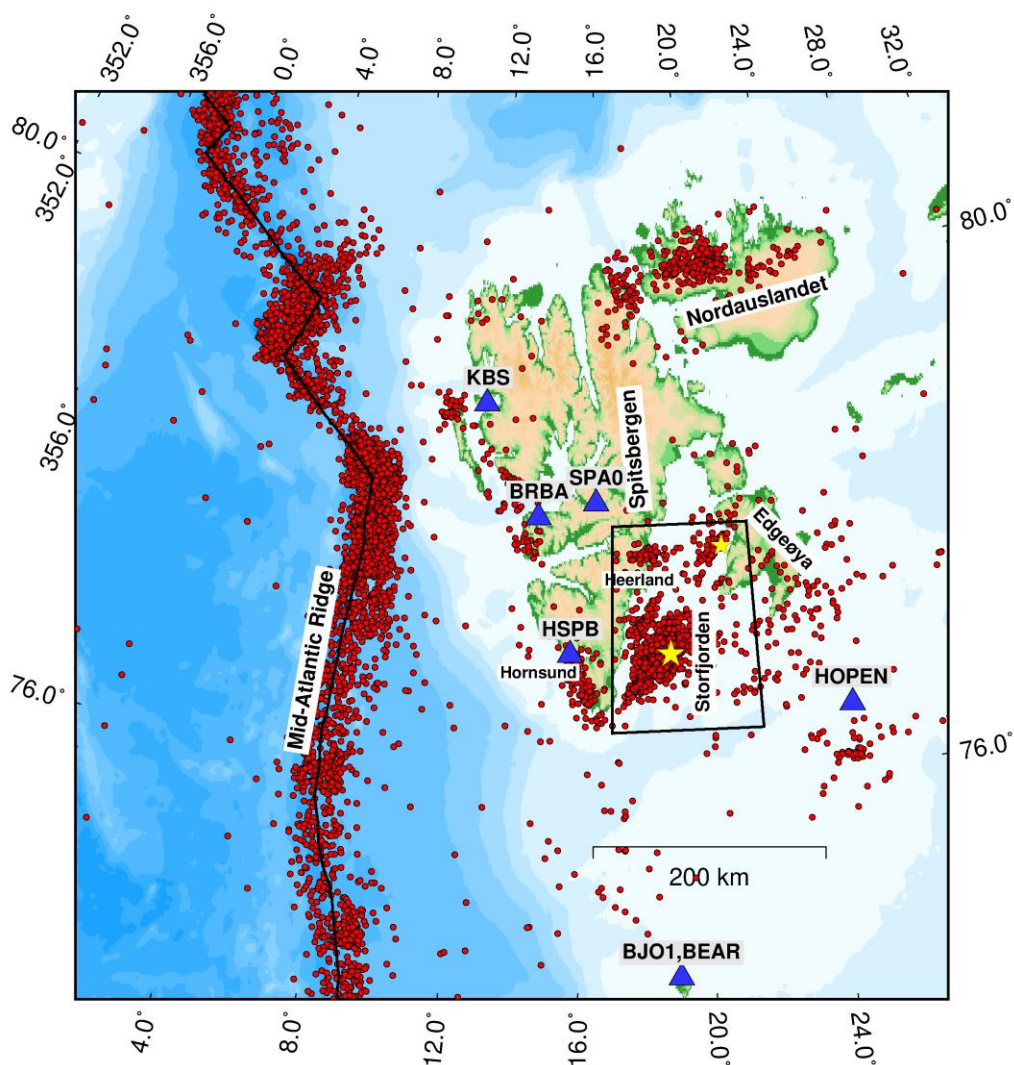
603

604   Figure 2. Seismicity (red circles) on the Mid-Atlantic ridge and Svalbard between 2008 and

605   2020 from the Norwegian National Seismic Network (NNSN) bulletin. The two largest events

606   in the sequence on 21 February 2008 (M_W 6.1) and 29 March 2016 (M_W 5.2) are plotted as

607   yellow stars. Permanent seismic stations within the area of this map are plotted as blue triangles

608   along with their station code. The area of the Storfjorden earthquake sequence is indicated by
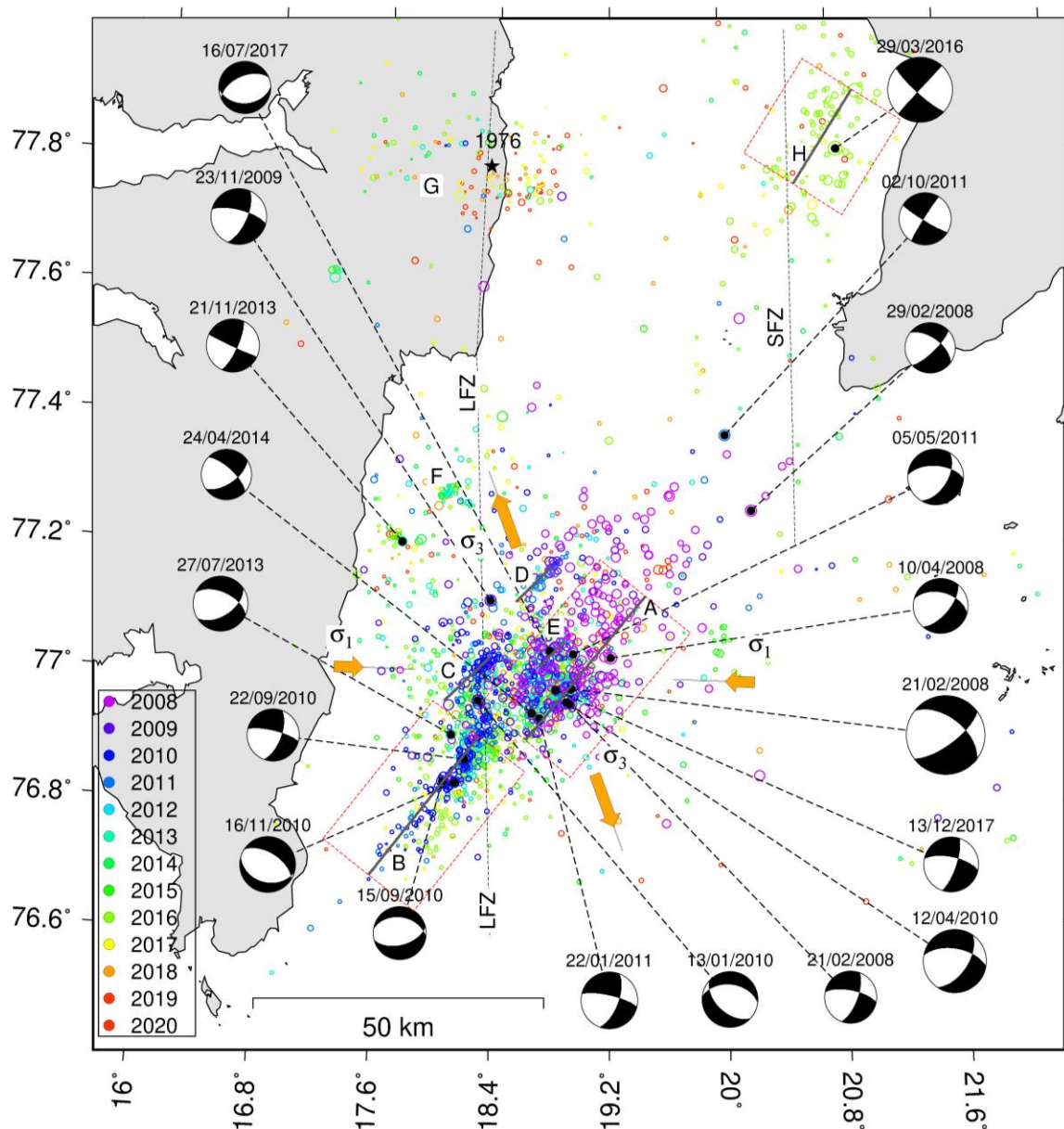
609   the black box.
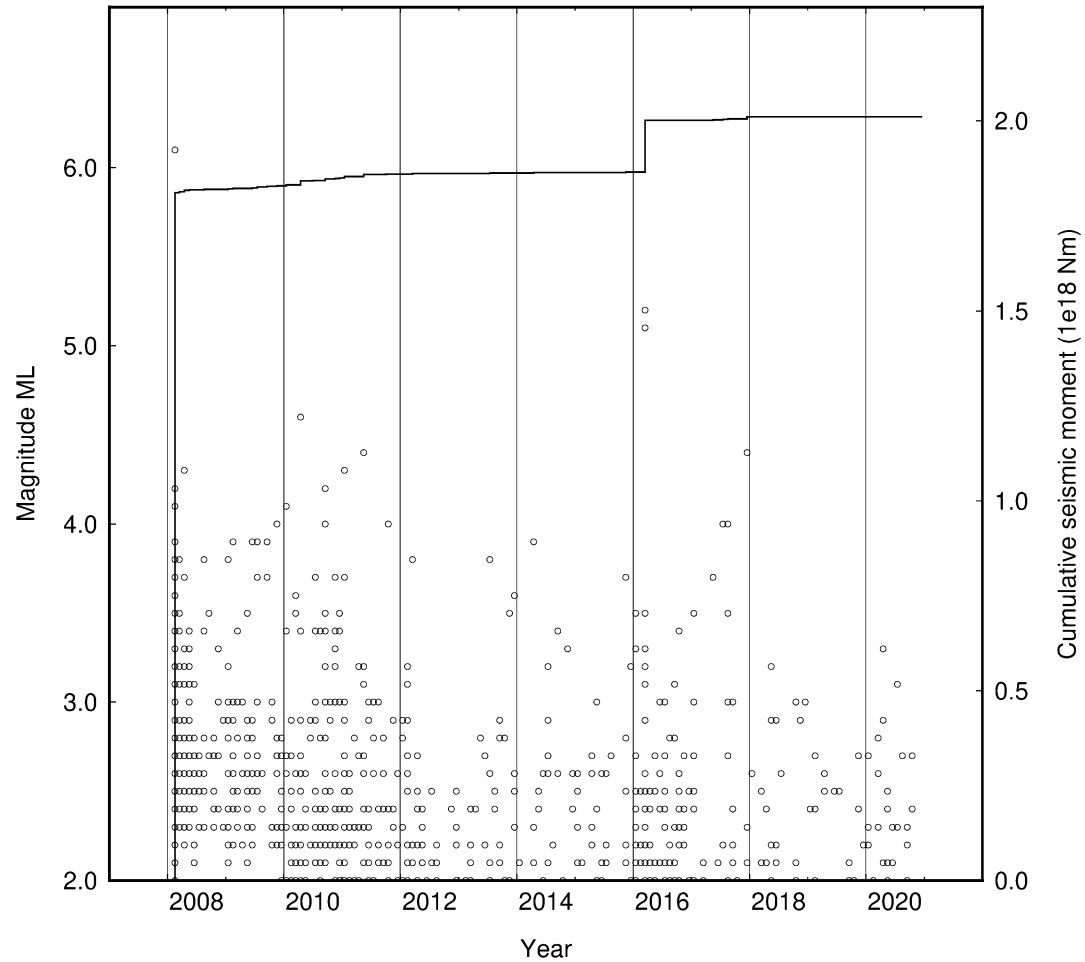
610

611

612

613   Figure 3. Distribution of magnitude M_L and cumulative seismic moment of the

614   Storfjorden earthquake sequence over time. Magnitudes are taken from the NNSN bulletin.

615

616

Figure 4. Map of relocated seismicity from 2008-2020 in Storfjorden together with double

couple mechanisms obtained through moment tensor inversion as given in Table 1. Epicenters

are plotted in color depending on the year of occurrence as given in the legend. The mechanisms

near the 2008 the mainshock area are oblique-normal, while they are pure strike-slip faulting

mechanisms for events north of the mainshock cluster. Linear features identified from the

seismicity distribution are indicated by solid black lines and labelled with letters (A-H). The

624   features A-F are repeated in Figure 5. The red boxes indicate the extent of the areas around

625   features A, B and H, respectively, from which events are selected for the projections in Figure

626   6. The directions of orange arrows indicate the trend of the greatest principal stress (σ_1) and the

627   least principal stress (σ_3) and their length is inversely proportional to the horizontal projection

628   of the plunge angles of the respective stresses axes. The thin lines beneath.the orange arrows

629   indicate the horizontal for plunge=0⁰.. The location of the 1976 Heerland earthquake is given

630   by a black star. The dashed lines indicate the assumed southward continuation of two fault

631   zones on either side of Storfjorden, LFZ and SFZ, with unknown positions and fault patterns.

632
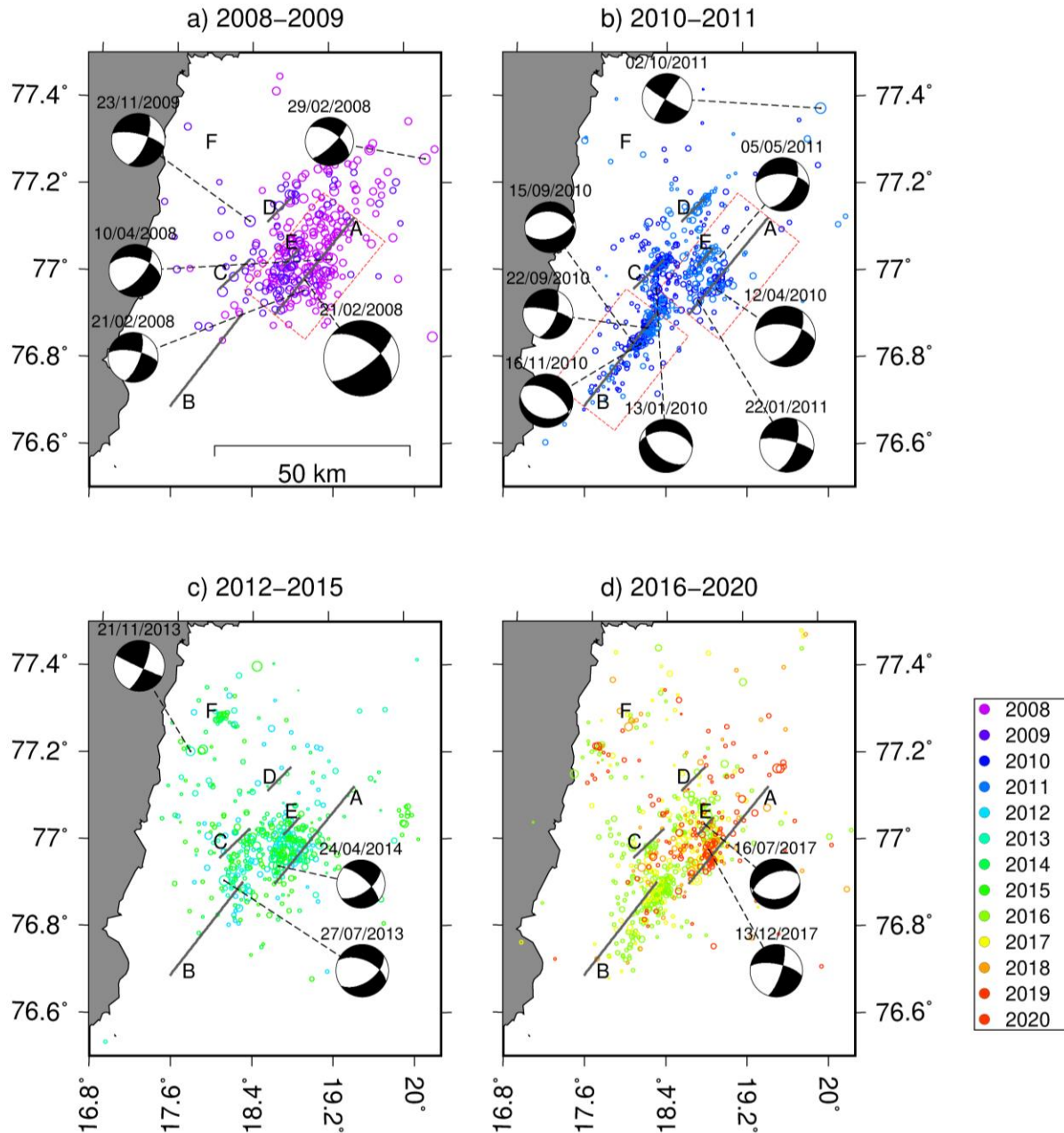
Figure 5. Main cluster seismicty relocated with double-difference method and fault plane

solutions for four different time periods as indicated on top of each map. Linear features

identified from the seismicity distribution are indicated by solid black lines and labelled with

letters (A-F). The four periods are: a) 2008-2009: the activity is focused around the 2008

mainshock; b) 2010-2011: the seismicity spreads to linear features (B-E); c) 2012-2015:

639   segment B is not very active, but to the northwest the cluster F appears; d) 2016-2020: previous

640   structures are still active, note that the activity to the northeast (H in Figure 4) is not included in

641   this map. Epicenters are plotted in color depending on the year of occurrence as given in the

642   legend. The red boxes indicate the extent of the areas around features A and B, respectively,

643   from which events are selected for the projections in Figure 6.

644
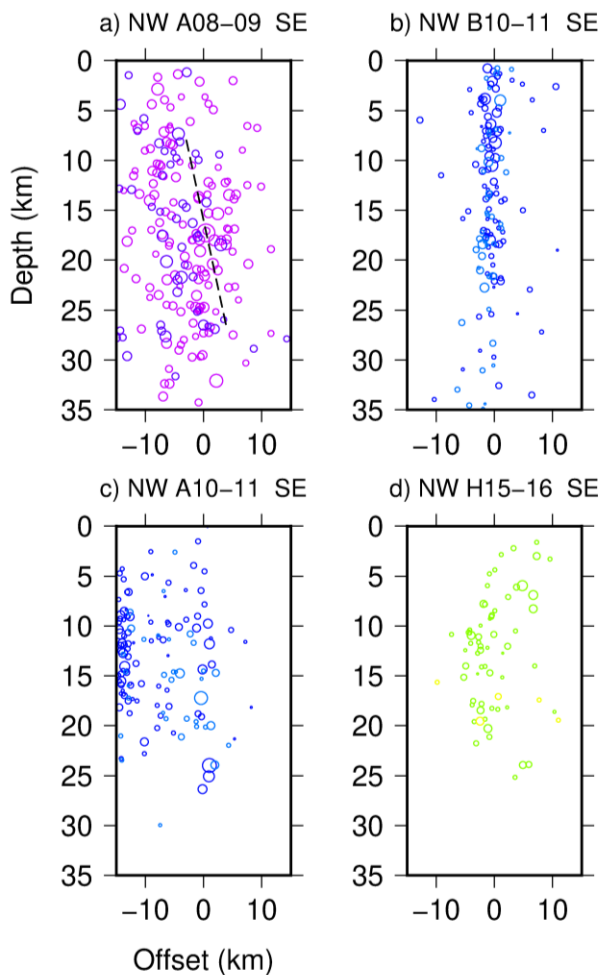
645

646   Figure 6. Projection planes perpendicular to features (A, B and H) that are indicated in Figures 4

647   and 5. Seismicity is projected (orthographic) onto planes perpendicular to the linear trends of

648   epicenters, which is roughly in NW-SE direction for all of them (Table S2). The four plots are:

649   a) section across feature A for years 2008-2009, the orientation of the main shock fault plane is

650   indicated by the dashed line; b) section across feature B for years 2010-2011; c) section across

651   feature A for years 2010-2011; d) section across feature H for years 2015-2016 (see Figure 4).

652   The color coding of the year is as in Figures 4 and 5.

653

654
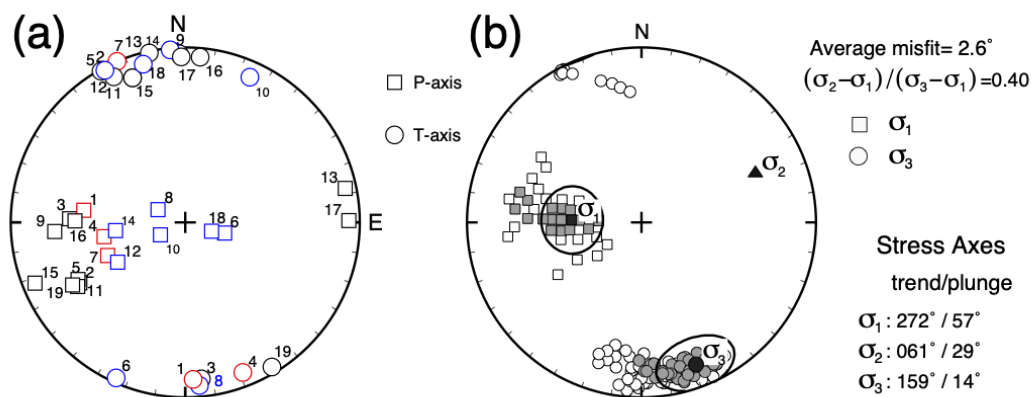
655

656

657   Figure 7. (a) Distribution of *P* axes (*squares*) and *T* axes (*circles*) of the 19 shocks of

658   Storfjorden earthquake sequence used for stress tensor inversion. Each *P*– and *T*–axis is

659   identified by the event id number listed in Table 1 and color coded for mechanism types:

660   oblique dip slip (*red*), normal faulting (*blue*) and strike-slip (*black*). (b) Orientations of σ_1 axes

661   (*squares*) and σ_3 axes (*circles*) of the 208 acceptable stress models of the stress inversion using

662   the 19 Storfjorden earthquake sequence data set. The best–fitting stress model (*black symbols*)

663   has an average misfit value of 2.6° and corresponding stress ratio, R = 0.40. The stress models

664   with 90% confidence limit is plotted with gray shaded symbols, whereas the open symbols

665   indicate 99% confidence limit and average misfits of about 4.0° and 4.5°, respectively.